Damage micromechanisms of stress corrosion cracking in Al-Mg alloy with high magnesium content

Hirayama, Kyosuke
Department of Mechanical Engineering, Kyushu University

Toda, Hiroyuki
Department of Mechanical Engineering, Kyushu University

Fu, Dongsheng
Department of Mechanical Engineering, Kyushu University

Masunaga, Ryohei
Department of Mechanical Engineering, Kyushu University

他

出版情報：Corrosion Science. 184, pp.109343-, 2021-05-15. Institute of Corrosion
バージョン：

Corrosion Science 184 (2021) 109343

Contents lists available at ScienceDirect

Corrosion Science

journal homepage: www.elsevier.com/locate/corsci

Damage micromechanisms of stress corrosion cracking in Al-Mg alloy with high magnesium content

Kyosuke Hirayama [a], Hiroyuki Toda [a,*], Dongsheng Fu [a], Ryohei Masunaga [a], Hang Su [a], Kazuyuki Shimizu [a,b], Akihisa Takeuchi [c], Masayuki Uesugi [c]

[a] Department of Mechanical Engineering, Kyushu University, 744, Motooka, Nishi Ward, Fukuoka City, Fukuoka 819-0395, Japan
[b] Department of Physical Science and Materials Engineering, Iwate University, 4-3-5 Ueda, Morioka City, Iwate 020-8551, Japan
[c] Japan Synchrotron Radiation Research Institute, 1-1-1, Kouto, Sayo-cho, Sayo-gun, Hyogo 679-5148, Japan

ARTICLE INFO

Keywords:
Stress corrosion cracking
Al-Mg alloy
Hydrogen embrittlement
Nanotomography
Phase-contrast imaging

ABSTRACT

Al-10Mg alloys, which are highly susceptible to SCC, were prepared with various β precipitate morphologies. Interrupted in-situ tensile tests were conducted under synchrotron X-ray radiation, employing a recently developed X-ray microtomography technique that combines high-energy, applicability to metallic materials, and ultra-high resolution. Preferential dissolution of the β phase along grain boundaries, and incidental intergranular and transgranular fracture, were observed in 3D. A drastic decrease in SCC resistance was measured after hydrogen charging. The additional effect of external hydrogen absorbed from an aqueous solution during loading was also revealed, by directly measuring crack-tip plasticity. The aquatic environment, one of the most extreme conditions for hydrogen uptake, caused continuous crack-tip corrosion. Catastrophic failure was observed when an alloy had both a relatively high areal grain boundary coverage by film-like β phase, and a reticulately interconnected plate-like β phase in the grain interior. Hydrogen bubble formation was also observed, in relation to the progress of crack-tip corrosion. The main corrosion product was identified as $Al(OH)_3$, based on its linear absorption coefficient. The respective amounts of corrosion products and hydrogen gas in the gas bubbles, and the pH value of the aqueous solution, were accurately measured during in-situ tensile testing, enabling estimation of the local elevation of hydrogen content in the crack-tip vicinity. Finally, a quantitative criterion for the occurrence of hydrogen embrittlement in inter-β ligaments is discussed, together with the applicability of the findings to the prevention of SCC.

1. Introduction

Al-Mg alloys are practically important medium-strength aluminum alloys, and have been widely used in building panels, ship construction, automobiles, welded structures for chemical plants, etc. Ordinary Al-Mg alloys are non-heat-treatable, relying on a combination of solid solution strengthening and work hardening. Representative alloys are A5052 and A5083 alloys with nominal magnesium contents of 2.2 ~ 2.8 and 4.0 ~ 4.9 mass%, respectively, which exceed the solubility limit of magnesium in aluminum at ambient temperature (~ 1.7 mass % [1]). It is known that increased magnesium content results in greater strength in Al-Mg alloys. Magnesium accounts for roughly 2% of the earth's crust, significantly higher than the major alloying elements (copper: 0.01%; zinc: trace) in high-strength aluminum alloys. Al-Mg alloys can therefore be assumed to be candidates to replace high-strength aluminum alloys. The former are, however, prone to stress corrosion cracking (hereinafter SCC) when the magnesium content is increased, and the susceptibility to SCC is positively correlated with magnesium content.

It has been well documented that SCC in Al-Mg alloys originates from hydrogen embrittlement. The most highly cited research was performed by Pickens et al. [2], in which they found greater susceptibility to intergranular SCC (hereinafter IGSCC) under mode I loading, compared to mode III loading, especially with the addition of a hydrogen recombination poison. In fact, it has been reported that IGSCC is enhanced after Al-Mg alloys are pre-charged with hydrogen [3]. It has also been reported that hydrogen plays a dominant role in the SCC of Al-Zn-Mg alloys [4]. It is known that the growth kinetics of environmentally assisted cracking is controlled by the relative humidity of humid air in Al-Zn-Mg alloys, and not associated with environmental molecular hydrogen gas [5,6]. This is because molecular hydrogen gas does not

* Corresponding author.
E-mail address: toda@mech.kyushu-u.ac.jp (H. Toda).

https://doi.org/10.1016/j.corsci.2021.109343
Received 19 July 2020; Received in revised form 4 February 2021; Accepted 22 February 2021
Available online 24 February 2021

readily dissociate on aluminum surface, while H_2O can be reduced to atomic hydrogen during surface oxidization when the surface oxide layer of an aluminum alloy is fragmented during external loading. The reaction between atmospheric water and aluminum produces hydrogen with extremely high fugacity (1.3×10^{50} atm) [7], which enables a considerable amount of hydrogen entry into the aluminum.

Another possible source of hydrogen-based SCC in aluminum alloys is the presence of pre-existing hydrogen. In general, aluminum has a large solubility gap (about 19 times difference) between the liquidus and solidus phases at the melting point [8]. In particular, it has been reported that magnesium makes the surface oxide layer more porous and permeable to hydrogen, thereby enhancing hydrogen absorption in Al-Mg alloys [9]. It has also been reported that adding magnesium increases the hydrogen solubility in liquidus aluminum [10]. In fact, the reported hydrogen content in a commercial Al-Mg alloy (A5083) is considerably higher than the equilibrium solubility of hydrogen in aluminum [11].

On the other hand, it has been well documented that supersaturated magnesium is precipitated as β-Al_3Mg_2 phase, based on the decomposition process: supersaturated α → GP zones → β" → β' → β [12]. Preferential precipitation of β phase is observed along grain boundaries because of the relatively large strain energy required for precipitation, which inhibits homogeneous nucleation for precipitation in the grain interior [13]. Subsequent precipitation in the grain interior is also observed, which exhibits precipitation hardening in an alloy. It has been reported that β' or β phase formed along grain boundaries often exhibit a continuous film when an alloy is aged at a moderate temperature [14]. For example, Pickens et al. aged an A5083 alloy for 72 h at 423 K and, using transmission electron microscopy (hereinafter TEM), observed a semi-continuous film-like β phase along the grain boundaries [2]. Crane et al. exposed an A5083 alloy for 30 months at 343 K, after which they observed, using TEM, that the grain boundaries were covered with a 30-nm thick β film, with an areal β film grain boundary coverage of 100% [15]. It is well known that the β phase is electrochemically less noble than the matrix aluminum [16]. According to an anodic polarization experiment performed by Jones et al., Al-Mg solid solution is more noble than the β phase, resulting in a relatively high galvanic potential of approximately 1 V between the A5083 and the β phase. It seems, therefore, most likely that preferential dissolution of the β phase occurs when grain boundary β phase is connected in a reticulate manner. Such film-like β phase is assumed, along with hydrogen embrittlement, to be one of the primary origins of IGSCC. The related aging treatments are therefore termed "sensitization" with respect to the SCC phenomenon in Al-Mg alloys.

Hydrogen is locally produced through a hydrolysis reaction originating in the β phase dissolution. Eborall et al. measured the hydrogen content of a corroded Al-5Mg alloy plate, and observed an increase in superficial hydrogen content of about 40 mol ppm due to corrosion [17]. Gas bubble formation in a solution is sometimes observed in the case of aqueous corrosion [18]. Using TEM, gas bubbles have also been observed embedded in aluminum grain boundaries. For example, Scamans et al. observed the initiation of hydrogen bubbles in an Al-5.11 Mg alloy after only 10 min of exposure to water vapor at 343 K [19]. It is reasonable to assume that hydrogen embrittlement is more apt to occur where such locally produced hydrogen is added to pre-existing hydrogen as clearly demonstrated in McMahon's recent work [20].

Susceptibility to SCC is strongly dependent on heat treatment conditions, with the highest susceptibility associated with β film grain boundary areal coverage of 100% [21]. In fact, fast crack propagation (1 ~ 100 nm/s) has been observed due to the anodic dissolution of the β precipitates. This fact might imply that the preferential dissolution of the β phase predominates in the SCC phenomenon when the β phase is completely continuous. On the other hand, Ohnishi et al. reported that stress corrosion life is drastically reduced (to about 1/1300th the original lifetime) when cathodic hydrogen charging is applied to an Al-8Mg alloy tempered to maximize SCC susceptibility [22]. In addition, Zhang et al. [23] and Macmahon et al. [24] have recently shown that SCC is observed even in AA5083 and AA5456 alloys with independent β-particles distributed with a high number density. IGSCC has also been observed, even without precipitation of the β phase, in a quenched Al-5Mg alloy [3,25]. Crane et al. hypothesized that β dissolution triggers rapid embrittlement of inter-β ligaments by locally generated atomic hydrogen, and at the same time triggers further α-Al dissolution, leading to occluded crack solution acidification necessary for major crack-tip hydrogen production [15,26]. Tanguy has concluded that the principal effect of β precipitation is simply to enable hydrogen absorption in a material [27]. Likewise, given the micromechanisms reported in recent literature [15], it would be reasonable to assume that both β phase dissolution and hydrogen embrittlement play specific and complementary roles in SCC in Al-Mg alloys. In fact, it has been reported that IGSCC proceeds orders of magnitude faster than intergranular corrosion for a variety of compositions and tempers, implying that the kinetics of IGSCC is not explained only with the anodic dissolution process of the β phase [28–30]. Although Al-Mg alloys with a variety of microstructural features have been experimentally investigated to date [15,16,20,24,26,30], it would be still valuable to determine how hydrogen embrittlement is involved in the SCC process.

Visualization techniques, such as scanning electron microscopy (hereinafter SEM) and light microscopy, have been widely used to study the micromechanics of various phenomena in materials science. Information on the process of fracture and chronology of fracture events is, however, not obtained using such conventional post mortem techniques. In the case of SCC, fractographic and microstructural information is especially scarce due to corrosion. Alternatively, the fracture process can nowadays be monitored in real time in 3D by employing state-of-art X-ray microtomography (hereinafter XMT), offering a rapid method for assessing fracture behavior at 1 μm spatial resolution [31–33]. If an objective lens such as a Fresnel zone plate (hereinafter FZP) is used for full-field X-ray microscopy, the spatial resolution in XMT can be readily improved by more than one order of magnitude [34]. More than a decade ago, employing nanotomography with FZP optics, the present authors visualized nanoscopic precipitates in an aluminum alloy in 3D [34]. The photon energy available for such nanotomography imaging was limited to 10 keV at the time [34], due to the difficulty in fabricating high aspect ratio FZPs [35]; and this is in turn imposed a rigid restriction on sample size (a rod with a diameter of 35.3 μm had to be used in [34], for example), so that in-situ mechanical testing was rarely performed.

A breakthrough in the FZP technique has recently been achieved, however, by Takeuchi et al., who developed so called apodization FZP, increasing the photon energy available for nanotomography experiments to 30 keV [36–38]. This technique may enable high-resolution visualization of both the β phase in Al-Mg alloys and microscopic fracture events in the vicinity of SCC cracks, in reasonably bulky specimens.

In the present study, Al-10Mg alloys, which are highly susceptible to SCC, were prepared with various β phase morphologies. Interrupted in-situ tensile tests were conducted under synchrotron X-ray radiation, after a certain number of corrosion pits had been introduced. As has been discussed by Gudla et al., it would be so-called environment induced cracking. Although fracture surface is not necessarily covered with corrosion products, we assume as an acceleration test of the SCC phenomenon. The local dissolution behavior of the β phase and incidental intergranular and transgranular crack propagation behavior were visualized in 3D at ultra-high resolution. In addition, the distributions of eroded β phase and corrosion products were directly visualized in another set of interrupted in-situ tensile tests, together with the formation of hydrogen gas bubbles in an aqueous solution. The increase in the local hydrogen content was then assessed quantitatively in relation to the overall hydrogen embrittlement behavior.

2. Experimental

2.1. Materials used

An Al-9.82 Mg alloy with a chemical composition of 0.63 Mn, 0.049 Cr, 0.031 Ti, 0.017 Si, 0.0007 Fe, 0.0002 Na, 0.0002 Ca, and balance aluminum in mass%, was prepared. A continuously cast billet of 95 × 95 × 500 mm was homogenized at 713 K for 48 h, and hot rolled at 523 K at a rolling reduction of 93%. The rolled billet was then thermally cycled in the laboratory, with a triangular waveform in vacuum (4×10^{-4} Pa), between 653 K and 753 K (12 cycles for 24 h in total), for dehydrogenation. This material contained particulate β phase (hereinafter PTLβ). In another series of samples, after thermal cycling, the billets were solution heat-treated at 733 K for 2 h, and some were then sensitized by applying aging treatment at 298 (i.e., RT) - 448 K for 10 - 2880 h after water quenching. This as-solution-treated material did not contain the β phase (hereinafter Nβ). The aged material, called FLMβ with reference to its film-like β phase along the grain boundaries, was classified into three classes: highly sensitized at 448 K for 100 h (hereinafter FLMβ(HS)), moderately sensitized at 353 K for 10 h (hereinafter FLMβ(MS)), and sensitized at a low level at 298 K for 2880 h (hereinafter FLMβ(LS))

Tensile specimens similar to those used in the previous study [33] (0.6 (width) × 0.6 (thickness) × 3 (length) mm in gauge section) were machined by employing the electro discharge machining (hereinafter EDM) technique, with tensile load applied in the longitudinal direction (LD). Transverse to longitudinal direction (TD) and normal to the longitudinal direction (ND) are also shown in Fig. S1. It was reported by the present authors that considerable hydrogen charging is produced by simply applying the EDM technique in water for specimen machining [39]. EDMed specimens were tested after storing for 4 days at room temperature in order to test specimens with almost homogeneous hydrogen distribution by considering a hydrogen diffusion coefficient at room temperature and specimen size. On the other hand, when EDM is performed in oil, hydrogen uptake does not occur. Thus, in the present study, in order to examine the effects of pre-existing hydrogen on SCC, PTLβ materials were prepared with and without hydrogen charging (hereinafter PTLβ-HH and PTLβ-LH, respectively, for the high and low hydrogen content), simply by altering the machining fluid (i.e., water or oil) during EDM. The total respective hydrogen content of materials HH and LH was measured to be 5.0 and 0.2 mass ppm, based on thermal desorption analysis. All the Nβ and FLMβ materials were machined by employing the EDM technique in water. In addition, in order to investigate the effect of the external environment, the tensile tests were performed both in an Ar gas atmosphere and in water. The difference in external environment is indicated by concluding parentheses, as in FLMβ (MS)-HH(Ar) and FLMβ(MS)-HH(WTR). All the sample preparation and environmental conditions are schematically summarized in Table S1 together with grain dimensions characterized with a SEM.

2.2. Preliminary treatment

In order to investigate the mechanical effects of corrosion pits and hydrogen generated due to corrosion, all the tensile specimens were immersed in water in advance for 16 h. In this way, corrosion pits of about 20 μm in depth from surface were introduced in the gauge section of each specimen. A typical corrosion pit is shown in Fig. S2, which was imaged with the projection-type XMT technique described below (Section 2.3.1). For material LH, another thermal cycling treatment was applied after this preliminary treatment (see Table S1), in order to eliminate the hydrogen generated during corrosion in the preliminary treatment. All the microstructural observations and the mechanical tests were performed after all the treatments.

2.3. 3D imaging

The XMT experiments were performed at beam line BL20XU of SPring-8. A monochromatic X-ray beam of 20 keV was produced by a liquid nitrogen-cooled Si (111) double crystal monochromator. A miniature material test rig was positioned on a rotational stage (Fig. S1) located approximately 80 m from the X-ray source. Two XMT set-ups were assembled at the same time in BL20XU, thereby enabling imaging techniques with different levels of spatial resolution and field of view for a single specimen. The imaging set-ups were switched within a few minutes by remotely advancing and retreating a CMOS camera, and a number of optical devices, to and from an optical axis. The entire specimen was imaged with the projection-type XMT technique at each applied load level, and then the main SCC crack and its vicinity was imaged with the imaging-type XMT technique at a higher magnification while maintaining applied displacement. The initial strain rate was set approximately to 3×10^{-3} s^{-1} under displacement control. The XMT scans were performed at successive increments of applied displacement, while holding a tensile specimen at a fixed applied displacement for 3.3 ks at each loading step. Actual image capturing was conducted at the end of the holding time for 3.2 min (projection-type) and 7.9 min (imaging-type) every time. The conventional filtered backprojection algorithm was employed to reconstruct image slices for both the absorption-contrast and phase-contrast images [40].

2.3.1. Projection-type XMT

A high-resolution projection-type XMT set-up was constructed by setting the first CMOS camera (ORCA Flush 4.0, Hamamatsu Photonics K. K.), with 4.0 megapixels, at a sample-to-detector distance, *L*, of 20 mm downstream with respect to the specimen (Fig. S3). An objective lens for visible light was used to fit an effective camera pixel size of 6.5 μm × 6.5 μm. A scintillator of 20 μm GAGG thickness was used, owing to its superior photon yield. All the devices were installed in the first experimental hutch of BL20XU. The absorption-contrast XMT technique was used for observing the cracks, pores, particles, corrosion products, and hydrogen bubbles in the entire specimen. The exposure time for each projection was 0.1 s, and a total of 1,800 projection images were captured to reconstruct a single 3D image at each load level. Isotropic voxels with 0.5 μm edges and a spatial resolution of 1.0 μm were achieved in the reconstructed slices.

2.3.2. Imaging-type XMT

The experimental set-up for the imaging-type XMT is also shown in Fig. S3. Köhler illumination [35] with a rotating condenser zone plate was used for the imaging-type XMT experiment, with an apodization FZP placed about 500 mm downstream from the specimen. The second CMOS camera (same product information as above) was set at an *L* of 165 m downstream from the specimen, in the second experimental hutch, in another building. In order to compensate for the lower contrast in the imaging-type XMT observation, a phase plate was placed at the back focal plane of the objective FZP (i.e., 500 mm behind the apodization FZP), thereby generating phase contrast in the X-ray microscopy [41]. The imaging-type XMT technique provides an ultra-high resolution of 0.19 μm, with isotropic voxels with 0.068 μm edges, enabling the observation of microcracks, cracks with small crack-tip opening displacement, and even the film-like β phase along the grain boundaries. Here, the exposure time for each projection was 0.25 s, and again a total of 1,800 projection images were captured to reconstruct a single 3D image at each load level.

2.3.3. 3D qualitative image analyses

To observe the morphologies of microstructural features with sub-voxel accuracy, facetted iso-intensity surfaces of pentagonal shape were computed on the basis of the Marching Cubes algorithm [42]. To suppress inaccuracies originating from image noise, only features over 27 voxels in volume were counted as particles and microvoids in the XMT images.

Precise image registration was performed before particle tracking, using a transformation matrix by which the sum of the distances

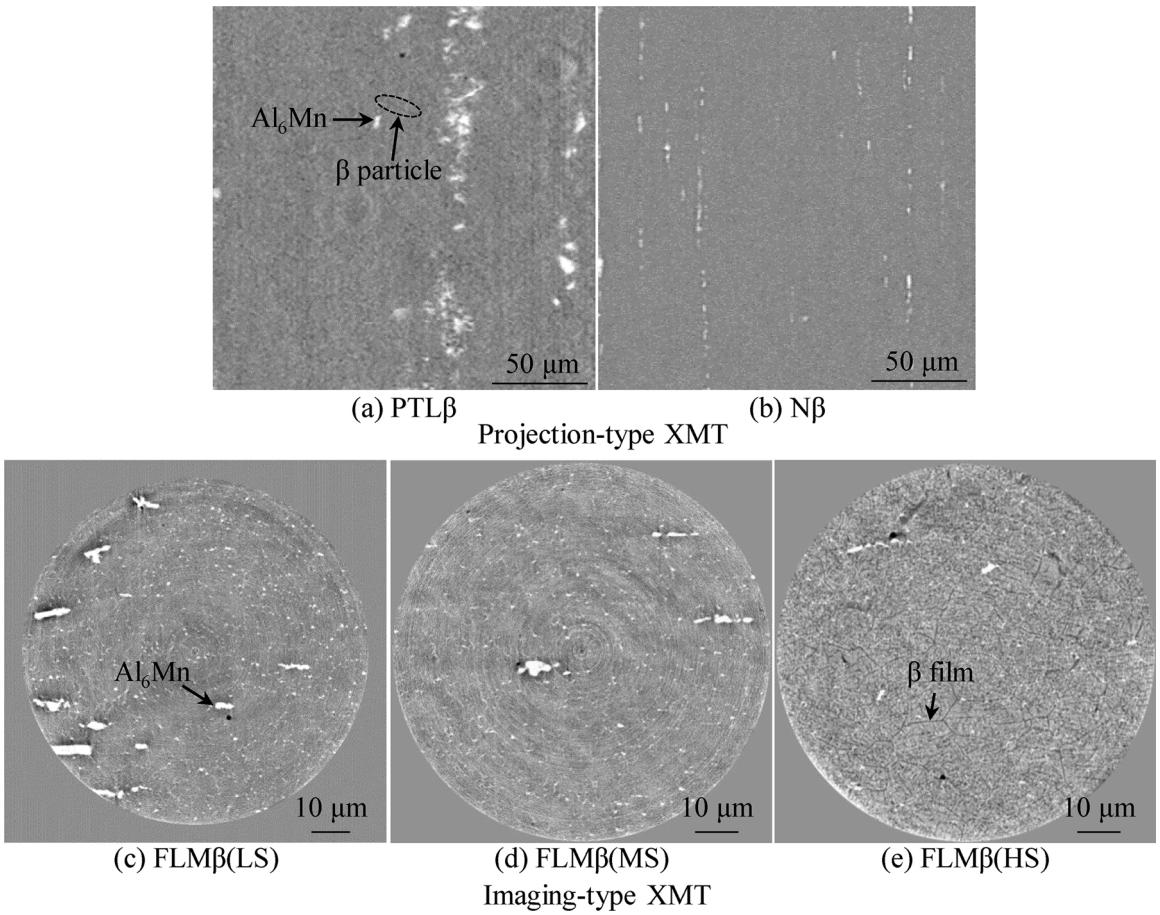

Fig. 1. 3D images of intermetallic particles in all the materials used. The major intermetallic particles observed were β-Al_3Mg_2 (i.e., the particulate or film-like phases darker than the aluminum matrix) and Al_6Mn (i.e., the white particulate phase). (a) - (b) and (c) - (e) were captured with the projection- and imaging-type XMT techniques, respectively, owing to the respective availability of the imaging techniques at different beam times. Although the difference in the imaging techniques yielded different levels of spatial resolution, it was confirmed that sufficient spatial resolution levels were applied for the respective materials.

between identical particles captured at neighboring loading steps was minimized. Particles were tracked in chronological order by employing the microstructural tracking technique [43]. The coefficients α, β, and γ in the matching probability parameter used in the microstructural tracking technique [44] were determined to be 0.8, 0.1 and 0.1, respectively, after systematically optimizing the conditions in a preliminary trial. 3D plastic strain distribution was then calculated by mapping the physical displacement of all the successfully tracked particles [43,44]. Note that according to the past report, the error in this particle tracking process is somewhat less than that of the spatial resolution of the projection-type XMT (i.e., approximately 1 μm) [43].

In addition, in order to examine the local deformation behavior at a propagating crack-tip, the mode I crack driving force was directly measured, in 3D reconstructed volume data, as a form of local crack-tip opening displacement (CTOD) [45]. The variation in CTOD was mapped along a crack-front line in high density.

2.4. Estimation of locally produced hydrogen due to anodic dissolution

In addition to the in-situ observation of tensile tests for the materials/conditions listed in Table S1, another set of experiments was performed, to estimate the amount of hydrogen locally produced due to the dissolution of the β precipitates and the α solid solution, resulting in hydrogen embrittlement. In this experiment, a tensile test of specimen FLMβ(HS)-HH(WTR), which had the highest pre-existing hydrogen content, and the highest expectation of hydrogen uptake from the aqueous solution, was performed in water.

The respective volume fractions of the β precipitates and α solid solution dissolved between neighboring loading steps (1.2 and 1.5% in applied tensile strain) were estimated by measuring the volume fractions of a visible corrosion product observed along the SSC cracks in two corresponding imaging-type XMT images. The chemical composition of the corrosion product was estimated based on its grey value in projection-type XMT images, thereby identifying the chemical formula for the actual anodic, cathodic, and hydrolysis reactions in the tensile specimen. In addition, hydrogen bubble formation was observed during the neighboring loading steps. Projection images were used to measure the diameters of spherical bubbles, and the amount of hydrogen gas was calculated. The aqueous solution environment was obtained by surrounding respective specimen gauge sections with a microdroplet. The water in the microdroplet was sucked up with a dropper immediately after the second XMT scanning was finished, and a pH meter specially designed for microdroplets (model New micro ToupH (Horiba, Ltd.)) was used to accurately determine the concentration of hydrogen ions in the solution.

The hydrogen locally produced due to the dissolution of the β precipitates and α solid solution is partitioned to the microdroplet as hydrogen ions, the hydrogen bubble as molecular gas, and the aluminum as solute atomic hydrogen. The amount of hydrogen produced, and the amount of partitioned hydrogen other than the solute atomic hydrogen, are precisely measurable as described above, and the amount of hydrogen absorbed into the alloy is thereby readily estimated.

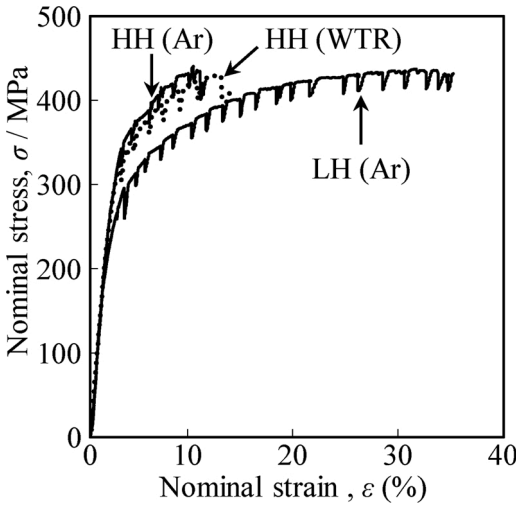

Fig. 2. Stress–strain curves recorded during the in-situ tensile testing of PTLβ material with different hydrogen contents and test environments.

3. SCC behavior

3.1. Materials with particulate β phase

Fig. 1(a) shows a virtual cross section of a projection-type XMT image of material PTLβ. Coarse β particles are extensively observed along the grain boundaries, as well as smaller β particles in the grain interior. The clustering of Al_6Mn particles (shown in white) is also observed, mainly along the grain boundaries, in a comparatively higher volume fraction. The spatial resolution of the projection-type XMT is approximately 1 μm, implying that even the β particles in the grain interior exceed 1 μm in size.

The stress-strain curves obtained during the in-situ tensile tests of material PTLβ (Fig. 2) represent the difference in SCC behavior among specimens PTLβ-LH(Ar), PTLβ-HH(Ar), and PTLβ-HH(WTR). PTLβ-LH (Ar) contained a negligible amount of pre-existing hydrogen, and its fracture behavior may therefore be inferred to have been affected solely by the existence of corrosion pits. First of all, it is noteworthy that SCC occurs even with particulate β, which is consistent to the recent reports by Zhang et al. [23] and Macmahon et al. [24]. Comparison of the three curves in Fig. 2 clearly indicates that the mechanical effect of the corrosion pits is not the major SCC mechanism in material PTLβ. Indeed, no SCC crack growth was observed in PTLβ-LH(Ar). It is noteworthy that when a tensile specimen was not held at a fixed applied displacement at each loading step, no SCC was observed. The additional effect of hydrogen uptake during the tensile test is included in the case of specimen PTLβ-HH(WTR) as compared to specimen PTLβ-HH(Ar). However, given that the size, number, and morphology of the corrosion pits are specimen-specific, there appears to be negligible difference between the two specimens in terms of SCC resistance, implying the importance of pre-existing hydrogen to SCC behavior in material PTLβ.

In order to examine the effect of the aquatic environment, a series of virtual cross sections during loading are shown in Fig. 3. The particles shown in white are Al_6Mn. The Al_6Mn particles highlighted by white arrows exhibit extensive cracking during loading, in advance of the crack-tip, in both materials. It appears that the cracks propagate by threading through cracked particles in advance of the crack-tip. Fig. 4 shows the 3D crack extension behavior and microvoid initiation / growth behavior that mainly originated from the Al_6Mn particles. It seems likely that the extent and distribution of damage evolution at the particles was not remarkably different in the two circumstances.

Although hydrogen is not visible using the conventional techniques of microstructural observation, indirect evidence of hydrogen embrittlement has been reported in the literature. One of the most characteristic features of materials undergoing hydrogen embrittlement is strain localization [46,47]. Employing a similar projection-type XMT technique, 3D strain distribution was observed by the present authors to be a characteristic feature of high strength Al-Zn-Mg alloys [46]. According to a recent report, the extent of strain localization during tension can be an index of the severity of hydrogen embrittlement [48,49]. For

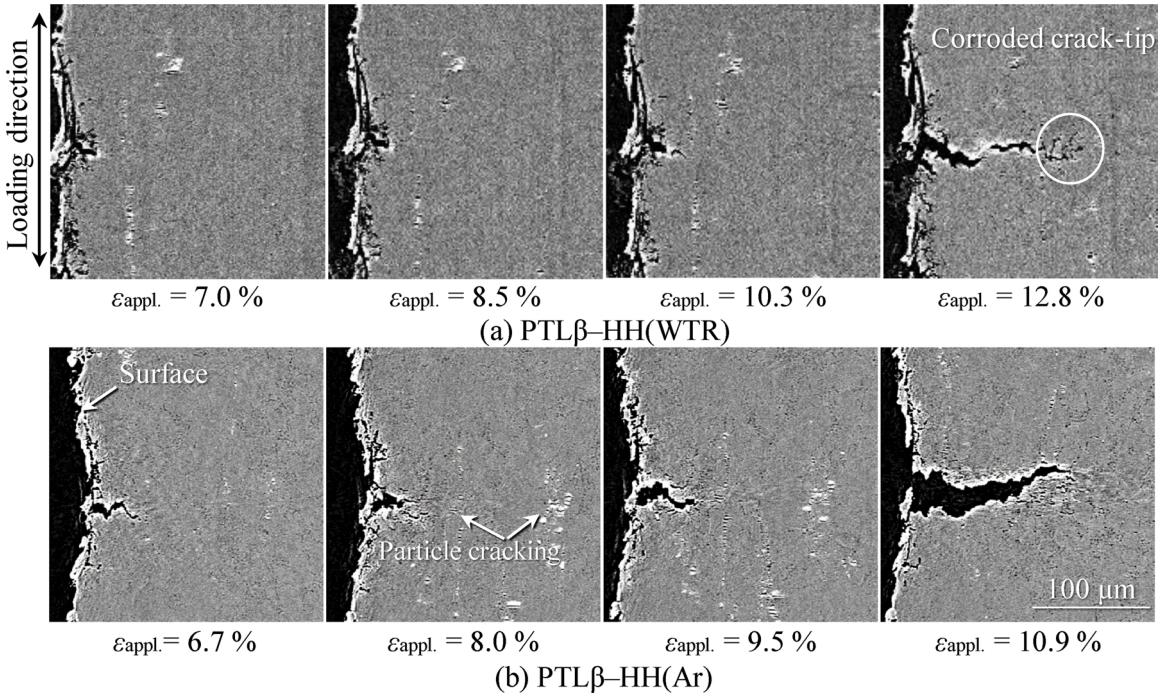

Fig. 3. Comparison of crack propagation behavior in materials with particulate β phase, tested both in water and Ar. Virtual cross sections obtained by the projection-type XMT technique are shown. The specimens shown in (a) and (b) were charged in advance with hydrogen. No crack initiation was observed in the case of specimen PTLβ-LH(Ar), which is therefore not shown here.

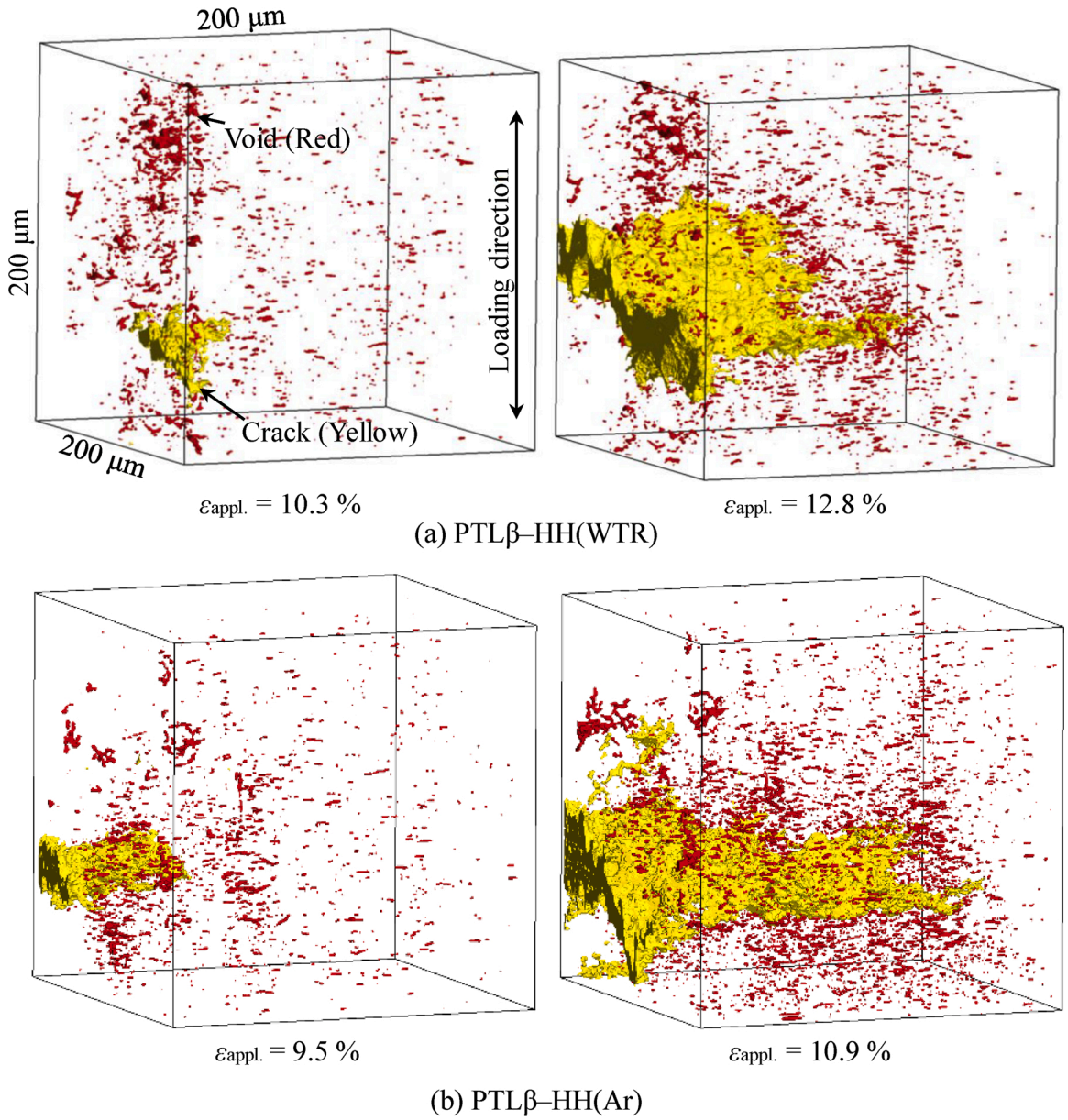

Fig. 4. Comparison of 3D crack propagation during damage evolution in specimens (a) PTLβ-LH(WTR) and (b) PTLβ-LH(Ar). The images were captured with the projection-type XMT technique. Both materials were charged with hydrogen in advance. Only the voids and crack (highlighted in red and yellow, respectively), have been segmented and shown here; the underlying aluminum matrix is not displayed.

example, when the total hydrogen content of an alloy is low, or when hydrogen is absorbed into dispersion particles even if the hydrogen content is high, strain localization is obviously suppressed. When an aluminum alloy susceptible to hydrogen embrittlement is exposed to tension, the strain is locally amplified several times, even during the macroscopic homogeneous deformation regime, before the maximum load [48,49]. Fig. 5 shows the 3D equivalent plastic strain distribution obtained, in the present study, by tracking particles in a series of 3D images, shown as virtual cross sections. Specimen PTLβ-LH(Ar) exhibits relatively uniform deformation as compared to the other two materials. It is, however, difficult to assess, based on Fig. 5, the relative severity of strain localization between specimens PTLβ-HH(Ar) and PTLβ-HH (WTR), due to very large local fluctuation.

Also noteworthy is that complicated crack-tip morphology is observed in the case of specimen PTLβ-HH(WTR), as highlighted by the white circle in Fig. 3(a). The characteristic crack-tip morphology of PTLβ-HH(WTR) is more distinctly demonstrated as the combination of a 3D image and corresponding virtual cross sections in Fig. 6. Part of the crack-front line is covered with corroded regions, as shown in Fig. 6(b) and (c) (highlighted in orange in Fig. 6(a)), where the crack-tip regions are bifurcated in complex and multiple ways. It appears that the bifurcated crack is mainly formed along the grain boundaries. Specimen PTLβ-HH(WTR) was kept in a water environment for 26.72 ks in total during the in-situ tensile test. The major focus of the in-situ experiments involving material PTLβ was confirmation that the hydrogen embrittlement behavior originated from pre-existing hydrogen, the only notable difference being the corrosion-assisted crack growth observed in PTLβ-HH(WTR), which implied that there are relatively certain effects of the aqueous solution on SCC behavior. Such time-dependent subcritical crack growth should be carefully separated from mechanical crack growth during loading. The former is inherent to the SCC behaviour in Al-Mg alloys, whereas the latter would be more or less specific to this idealized model experiment. The corrosion behaviour, which is mainly originated from the β dissolution, is one of the important mechanisms

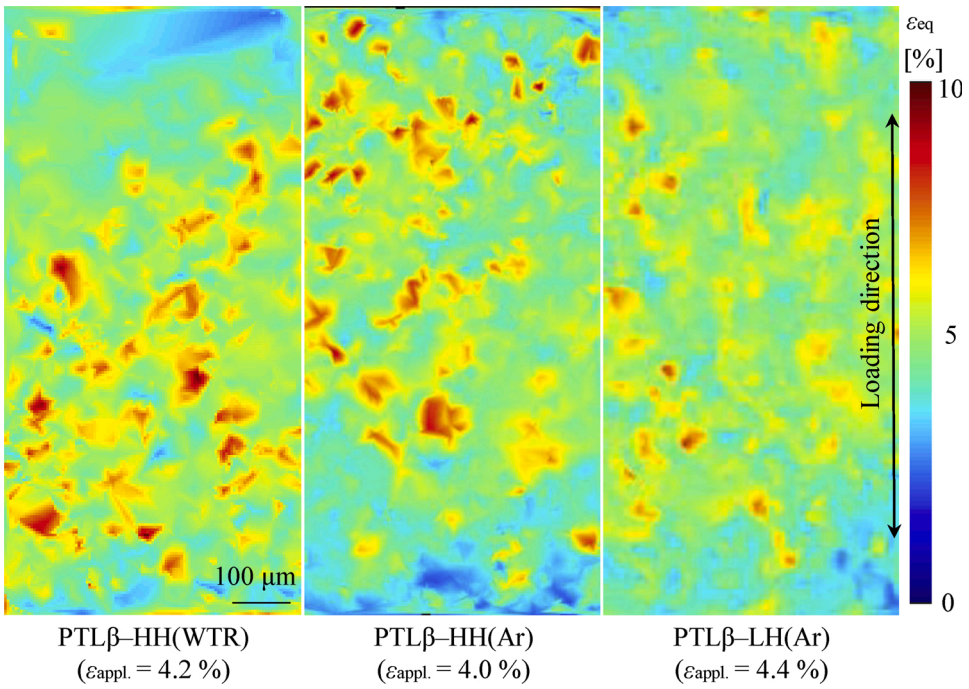

Fig. 5. 3D equivalent strain distributions measured during tension by tracking constituent particles. The strain distributions are represented on virtual cross sections in the 3D data sets.

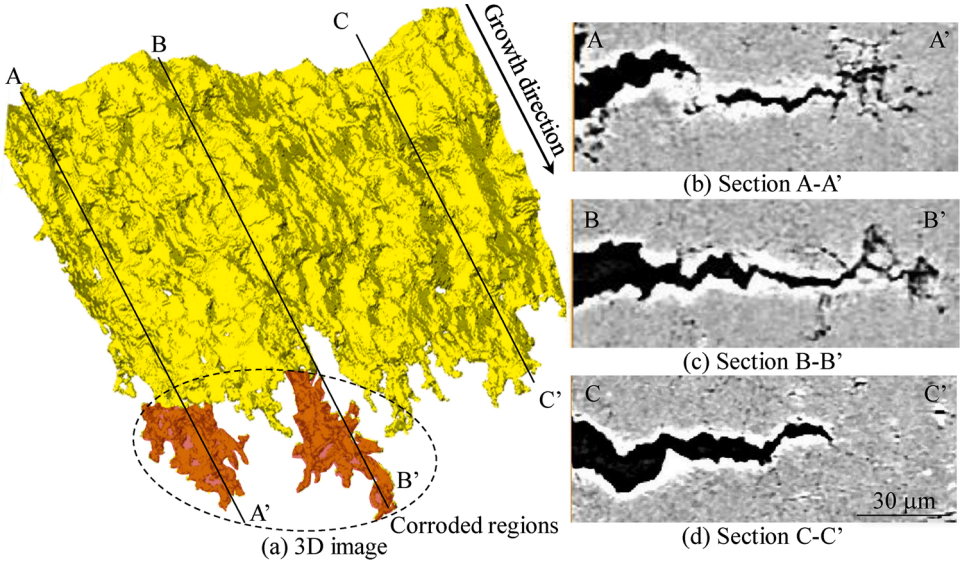

Fig. 6. 3D crack-tip morphology of a crack in specimen PTLβ-HH(WTR), at an applied strain of 12.8%: (a) a 3D image; (b) - (d) virtual cross sections corresponding to sections A-A', B-B', and C-C' in (a). The effects of corrosion are observable in some of the crack-tip regions, highlighted in orange in (a).

for the subcritical crack growth. Another mechanism is hydrogen embrittlement, which usually need time necessary for hydrogen to accumulate in the vicinity of a crack-tip. Fig. 7 shows an ultra-high resolution 3D image captured with imaging-type XMT. Particulate β phase is distributed somewhat discontinuously along the grain boundaries. A video highlighting the crack and particle distribution is included in the supporting information (Video S1). The video clearly demonstrates that the β particles are plate-like, and appear almost but not completely interconnected in a reticulate manner along the grain boundary planes. There appears to be rather limited uncracked ligaments on the crack planes, implying that a combination of preferential dissolution of the β phase and subsequent inter-β cracking results in cracking along the grain boundary planes.

To better evaluate the effect of the aqueous solution, CTOD was directly measured from the 3D images (Fig. 8). As is well known, CTOD is a fracture mechanics parameter with unique relationships with other fracture mechanics parameters such as the stress intensity factor and J integral. In general, the higher the CTOD, the more extensive is the crack-tip plastic deformation. The results in Fig. 8 should, however, be interpreted with caution because, as is shown in Fig. 3, the crack-tip morphology in material PTLβ is affected by two phenomena: crack-tip corrosion and crack-microvoid coalescence. The data points representing the former and latter phenomena are highlighted in black and red, respectively, in Fig. 8. Eliminating such singular data points indicates that CTOD is more remarkably varied in specimen PTLβ-HH(WTR) than in specimen PTLβ-HH(Ar), likely due to some hydrogen-dislocation

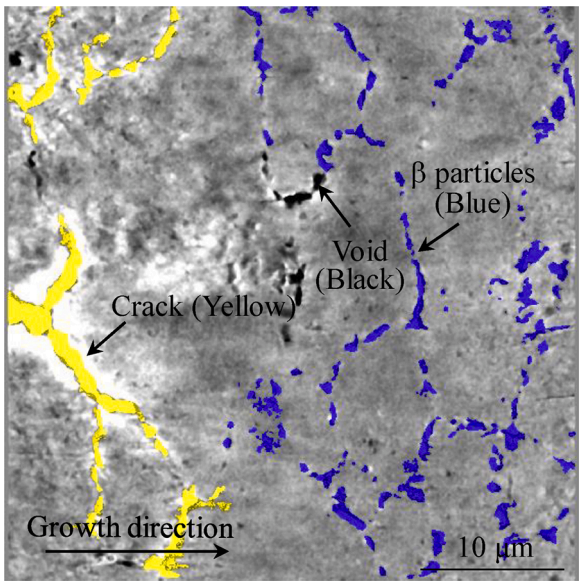

Fig. 7. Ultra-high resolution 3D image of crack-tip corrosion in specimen PTLβ-HH(WTR).

interaction, perhaps involving the hydrogen-enhanced local plasticity mechanism [46,47]. Crack-tip corrosion was observed in PTLβ-HH (WTR) as is indicated in Figs. 6 and 7. It is to be noted that especially large CTOD values are observed in the vicinity of the corroded regions (highlighted by three arrows in Fig. 8(a)). This difference can be associated with the enhancement of crack-tip plastic deformation due to the increase in local hydrogen content near the corroded crack-tip, which is caused by in-situ hydrogen uptake from the water.

3.2. *Materials with film-like β phase*

Fig. 1(b)–(e) show virtual cross sections of projection-type and imaging-type XMT images of materials Nβ and FLMβ. In material FLMβ (HS), β films exhibiting reticulate structures are observed along the grain boundaries, as well as aligned plate-like β particles in the grain interior, implying that the thickness of the β film exceeds the spatial resolution level of the imaging-type XMT (roughly 0.1 μm). On the other hand, no β phase is observed in materials Nβ, FLMβ(LS), or FLMβ(MS) at the spatial resolution level of the imaging-type XMT. Although not shown in the figures due to space limitations, even SEM imaging revealed no β phase in these three materials. It is reasonable to assume that there is actually no β phase in material Nβ. According to the TEM observation by Yi et al., the thickness of the β phase varies between 5 and 30 nm during aging at 343 K, between 720 and 21600 h, in an Al-4.4 Mg alloy [50]. It is reasonable to assume that the thickness of the β phase would have been well below 10 nm in materials FLMβ(LS) and FLMβ(MS). It has been reported that sensitization to SCC occurs when a material with a Mg content of approximately 3 mass% or more is exposed between 323–498 K [15]. Employing TEM at a moderate magnification (about × 66,000 in the published paper) Tanguy et al. observed an Al-5Mg alloy that had been aged at room temperature for 16 years, and concluded that the grain boundaries were free of precipitation [3]. It is however to be noted that the Mg content was higher in the materials used in the present study than those reports, implying that the above-mentioned estimations may be more or less underestimated due to this difference.

The stress-strain curves in Fig. 9, obtained during the in-situ tensile testing of materials Nβ and FLMβ, represent the difference in SCC behavior among specimens Nβ-HH (Ar), Nβ-HH (WTR), FLMβ(LS)-HH (WTR), FLMβ(MS)-HH(WTR), and FLMβ(HS)-HH(WTR). Fig. 10 shows SEM fractographs of the three materials with film-like β phase (specimens FLMβ(LS)-HH(WTR), FLMβ(MS)-HH(WTR), and FLMβ(HS)-HH (WTR)). The fracture strain shown in Fig. 9 is in qualitative agreement with the thickness of the grain boundary β film, with conspicuous reduction in the fracture strain being seen in the case of specimen FLMβ

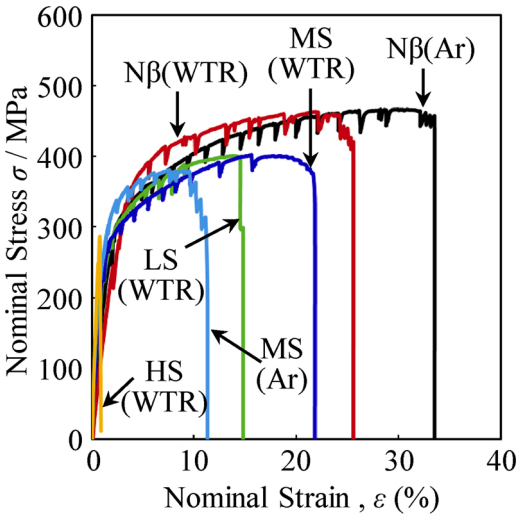

Fig. 9. Stress-strain curves recorded during the in-situ tensile testing of materials Nβ and FLMβ with different hydrogen contents and test environments.

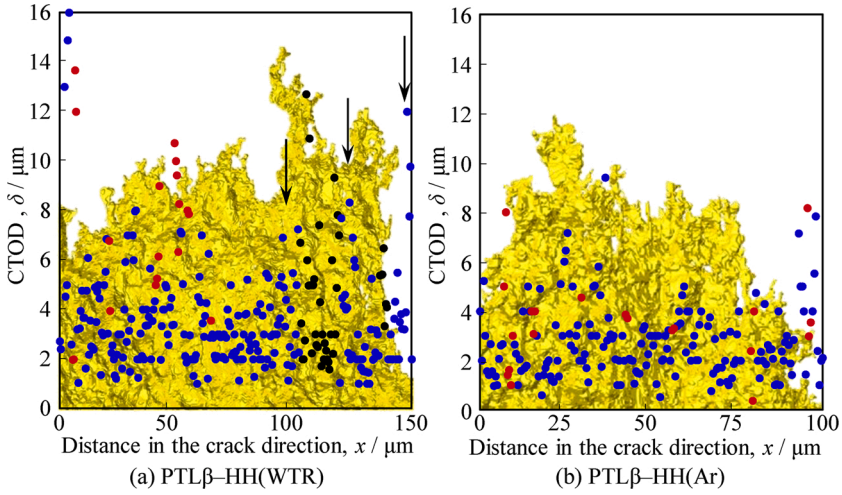

Fig. 8. Crack-tip opening displacement (CTOD) measured as an index of near-tip plastic deformation, which is usually enhanced by the effects of hydrogen. Data points where crack-tip corrosion and crack-microvoid coalescence are observed are highlighted in black and red, respectively, while data points showing no such external effects are shown in blue. The background yellow images are 3D crack images aligned with the horizontal axes. The applied strain levels were 12.8% and 10.9% in specimens PTLβ-HH(WTR) and PTLβ-HH(Ar), respectively.

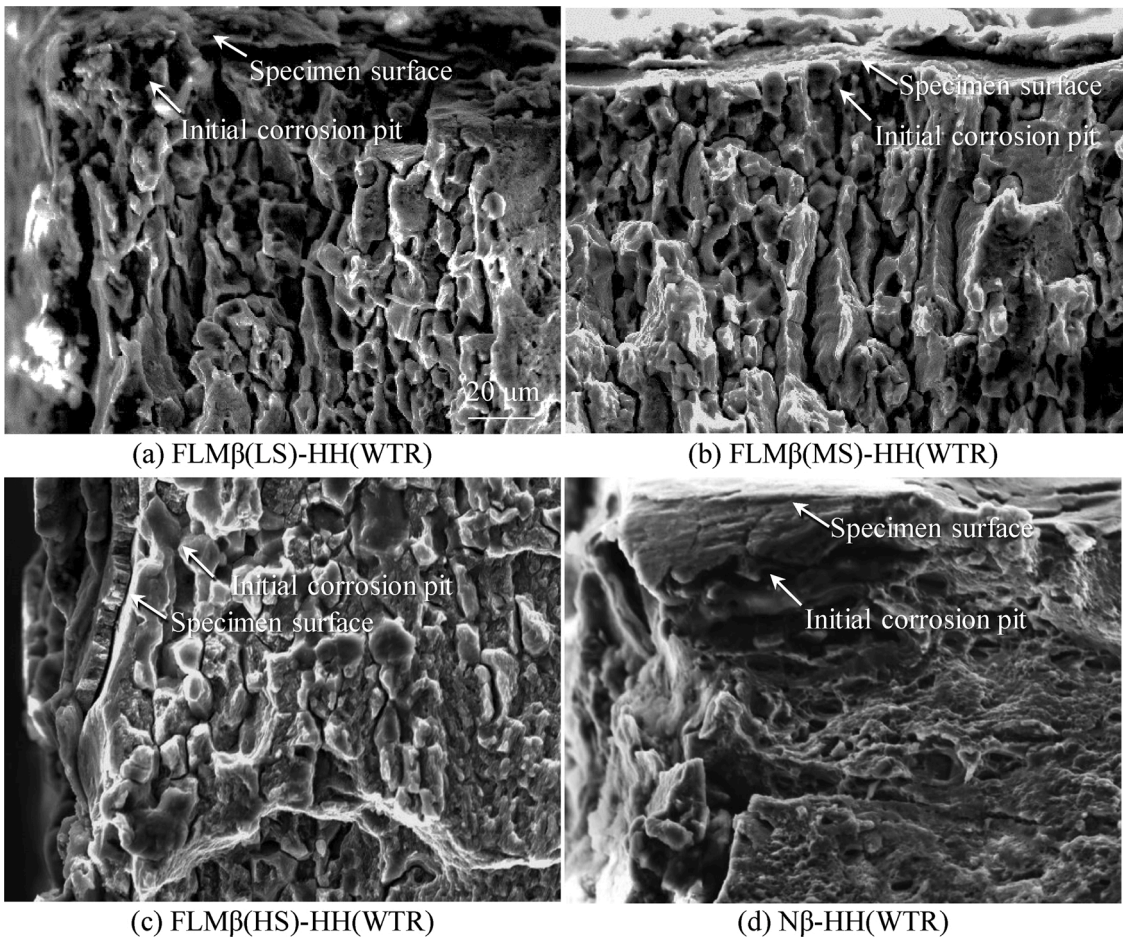

Fig. 10. SEM fractographs of FLMβ material with different degrees of sensitization, and specimen Nβ-HH(WTR). Specimens FLMβ(LS)-HH(WTR) and FLMβ(MS)-HH (WTR) exhibit intergranular fracture in the vicinity of the crack initiation points, whereas a mixture of intergranular and transgranular fracture modes is observed in specimen FLMβ(HS)-HH(WTR).

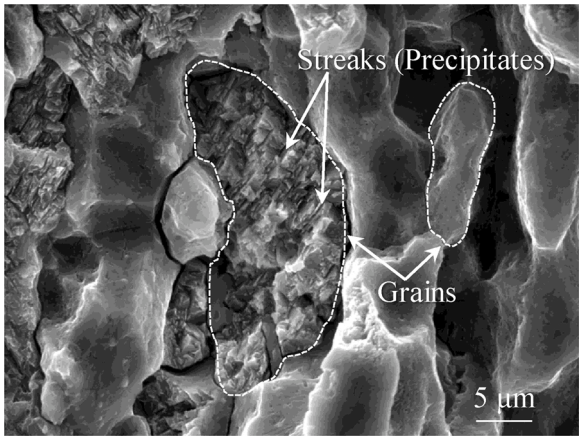

Fig. 11. Magnified view of Fig. 10 (c).

(HS)-HH(WTR), implying that its fracture mode might be different from those of the other specimens. Specimen FLMβ(LS)-HH(WTR) exhibits notable degradation in elongation compared to Nβ-HH(WTR). Although the aging time for material FLMβ(LS) was approximately 2% of that employed for the material in Tanguy et al.'s abovementioned study, it is reasonable to assume that nanoscopic precipitates formed along the grain boundaries on the length scale of a few angstroms to a nanometer, due to the high Mg content. The SEM fractographs revealed that specimen Nβ(WTR)-HH exhibited a transgranular dimple pattern, whereas FLMβ(LS)-HH(WTR), FLMβ(MS)-HH(WTR) and FLMβ(HS)-HH (WTR) exhibited intergranular fracture. Fig. 11 shows a magnified view of Fig. 10 (c). It is interesting to note that a characteristic transgranular fracture surface is observed only in specimen FLMβ(HS)-HH(WTR). The streaks embedded in the grain interior are aligned in two perpendicular directions in each grain. According to the current literature, the orientation relationship between the β phase and α-aluminum matrix in β-Al_3Mg_2 precipitates is: $(111)_\beta$ // $(001)_\alpha$ and $[110]_\beta$ // $[010]_\alpha$ [51]. It is therefore inferred that the streaks observed in Fig. 11 correspond to two different variants of the β-Al_3Mg_2 precipitates.

Fig. 12 shows the initial corrosion pit (Fig. 12(a)) and subsequent crack propagation behavior (Fig. 12(b) - (g)) in specimen FLMβ(MS)-HH (WTR), observed with the ultra-high resolution imaging-type XMT. The initial corrosion pit appears to be patchy and basically intergranular, with another characteristic feature being the formation of slender protrusions, likely along crystallographic triple junction lines, implying that local dissolution of the β phase occurs preferentially. Fig. 13(a) shows an interpretation of the 3D image shown in Fig. 12(a), with the triple junction lines highlighted in different colours. It has been reported that the β phase is discontinuous along grain boundaries in the case of aging below 373 K [15] or 473 K at the highest [26]. Since hydrogen embrittlement does not occur without loading, a fractional area of the patchy intergranular damage might correspond to β film areal coverage of the grain boundaries, which dissolves in the water during aquatic immersion. The subsequent loading in the aqueous solution mainly causes dissolution of the β film along the grain boundary plane, as shown

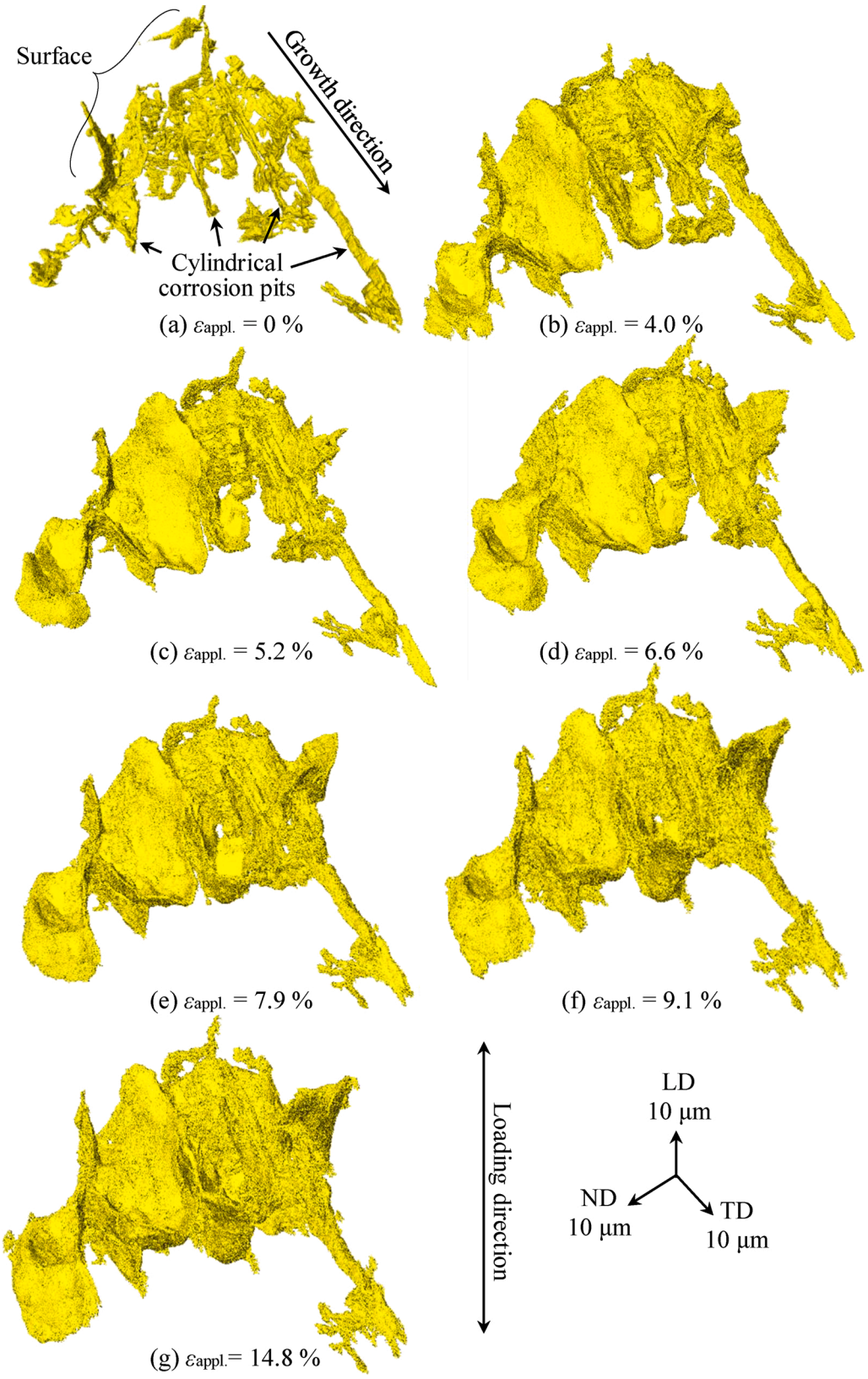

Fig. 12. High resolution crack initiation and propagation behavior in specimen FLMβ(MS)-HH(WTR), visualized with the imaging-type XMT technique.

in Fig. 13(b). The wedge that curves along the grain boundaries advanced incrementally during specimen observation. A video highlighting the crack morphology at an applied strain of 14.8% (Figs. 12(g) and 13 (b)) is included in the supporting information (Video S2). It clearly demonstrates that the crack face passes completely through the grain boundaries, implying that the crack extension is effectively assisted by hydrogen embrittlement.

As described above, specimen FLMβ(HS)-HH(WTR) exhibited mixed-

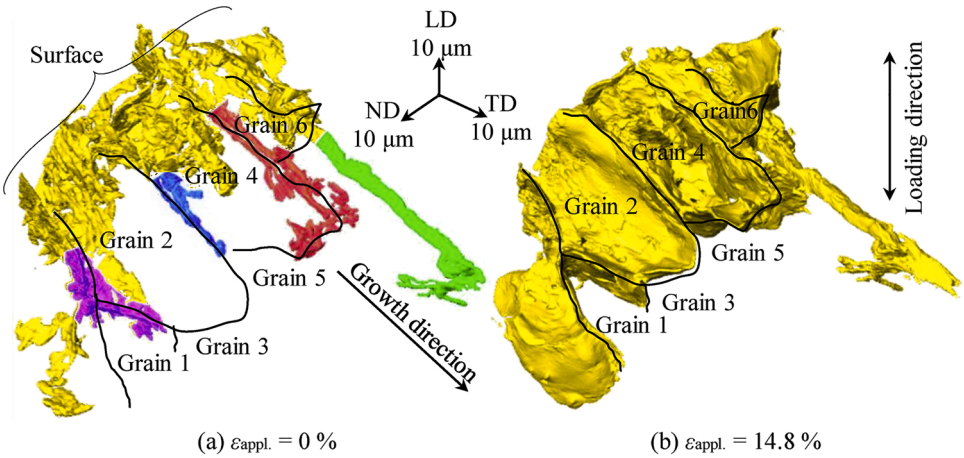

Fig. 13. Interpretations of 3D images shown in Fig. 12, with respect to underlying grain structure.

mode fracture, roughly half transgranular and half intergranular (as shown in the magnified view in Fig. 14), together with the considerably reduced elongation shown in Fig. 9. Based on the 3D and 2D images in Fig. 14(a) and (b), respectively, it seems most likely that the SCC cracking in FLMβ(HS)-HH(WTR) involved competition between inclined intergranular failure paths and almost horizontal transgranular failure paths, as shown in Fig. 14(b). A transgranular crack segment (highlighted in red in Fig. 14(a)) appears continuous, with no uncracked ligament. The blue crack segment in Fig. 14(a) is also transgranular, with the fracture path appearing to primarily reflect linkage of plate-like precipitates in the grain interior. It can be inferred that, in material FLMβ(HS), the grown precipitates are remarkably coarse and almost interconnected with each other. The interconnected precipitates have probably been dissolved out through the grain boundary crack, resulting in a more horizontal crack path with significantly reduced crack propagation resistance than the grain boundaries.

4. Hydrogen generation and uptake

4.1. Chemical formulae for hydrogen generation and uptake

Since the α−Al is more noble than the β phase, the β phase exposed to the aqueous solution is easily dissolved. When grain boundary β phase is film-like and interconnected, preferential dissolution of the β phase occurs, with the following anodic reactions [52,53]:

$$Mg \rightarrow Mg^{2+} + 2e^{-}, \quad (1)$$

$$Al \rightarrow Al^{3+} + 3e^{-}. \quad (2)$$

This is followed by further the progress of Reaction (2), where the α−Al is exposed to the aqueous solution in the vicinity of a crack-tip and on the crack surfaces. A possible cathodic reaction would be as follows [3,15,54]:

$$H_2O + e^{-} \rightarrow H\,(\uparrow) + OH^{-}. \quad (3)$$

Another cathodic reaction assumed to take place in the SCC of Al-Mg alloys (i.e., $H_2O + O_2 + 4e^{-} \rightarrow 4OH^{-}$) did not occur in the present experiment, because the SCC cracks were shielded from oxygen gas in the atmosphere by the surrounding aqueous solution. It has been reported that a number of possible cation hydrolysis reactions can cause the formation of principal corrosion products, depending on the pH of the solution [52,55]; these include:

$$2Al^{3+} + 3H_2O \rightarrow Al_2O_3 + 6H^{+}, \quad (4)$$

$$Al^{3+} + 3H_2O \rightarrow Al(OH)_3 + 3H^{+}. \quad (5)$$

The formation of aluminum hydroxide oxide (AlOOH) has also been reported as a hydrolysis reaction [57].

In order to identify the corrosion product formed in the present study, the linear absorption coefficient of a sample corrosion product was measured in a projection-type XMT image (Fig. 15), with the 8-bit grey values in the image being linearly proportional to the linear absorption coefficient, μ. The μ values for aluminum, the β phase, and the three corrosion products (Al_2O_3, $Al(OH)_3$, and AlOOH) are 9.29, 7.17, 8.80, 4.20, and 6.19 cm^{-1}, respectively. The measured linear absorption coefficient of the sample corrosion product was 3.81, which is comparatively close to that of $Al(OH)_3$. A magnesium-bearing corrosion product, such as magnesium hydroxide ($Mg(OH)_2$: μ =3.87 cm^{-1}), is also expected to be formed, stemming from the preferential dissolution of the β phase. The difference in μ between $Al(OH)_3$ and $(Mg(OH)_2$ is less than 10%, making segmentation in the 3D images physically difficult. Furthermore, the corrosion product shown in Fig. 15 is several tens of times thicker than that of the film-like β phase seen in Fig. 1(e). It is therefore most likely that the formation of $Mg(OH)_2$ would have been negligible compared to formation of Al^{3+} from the α-Al dissolution, within the volume measurement accuracy of the present study.

4.2. Estimation of crack-tip hydrogen uptake

Hydrogen bubbles were observed during the in-situ tensile testing of specimen FLMβ(HS)-HH(WTR), as shown in Fig. 16(a). The hydrogen bubbles appeared almost spherical, as illustrated in the magnified cross section in Fig. 16(b). The growth of the hydrogen bubbles was monitored with projection images, which confirmed that neither bubble flotation nor coalescence of neighboring bubbles occurred during the observation. The diameter of the hydrogen bubbles was measured using the projection images, and their internal gas pressure was estimated from the Young-Laplace equation, assuming the surface tension value of water to be 72.8 mN/m. The amount of hydrogen gas in the bubbles was calculated assuming the ideal gas law. The hydrogen gas production for the SCC crack shown in Fig. 17 was estimated to be 6.6×10^{-12} mol. The volume of the corrosion product (highlighted in purple in Fig. 17) increased, for the SCC crack shown in Fig. 17, from 2272.4–2523.2 μ m^3, between applied tensile strains of 1.2 and 1.5%. Assuming that the corrosion product consisted solely of $Al(OH)_3$, the increase in $Al(OH)_3$ was 7.1×10^{-12} mol between these two applied tensile strain values. According to Eq. (5), this indicates that 2.1×10^{-11} mol of hydrogen ions was produced at the same time. The pH value of the aqueous solution (43 μL in volume) decreased with increasing amount of corrosion product, from 6.5 to 5.9, implying that 3.7×10^{-12} mol of hydrogen was dissolved in the aqueous solution in the form of hydrogen ions. As a result, the amount of atomic hydrogen absorbed into the alloy was

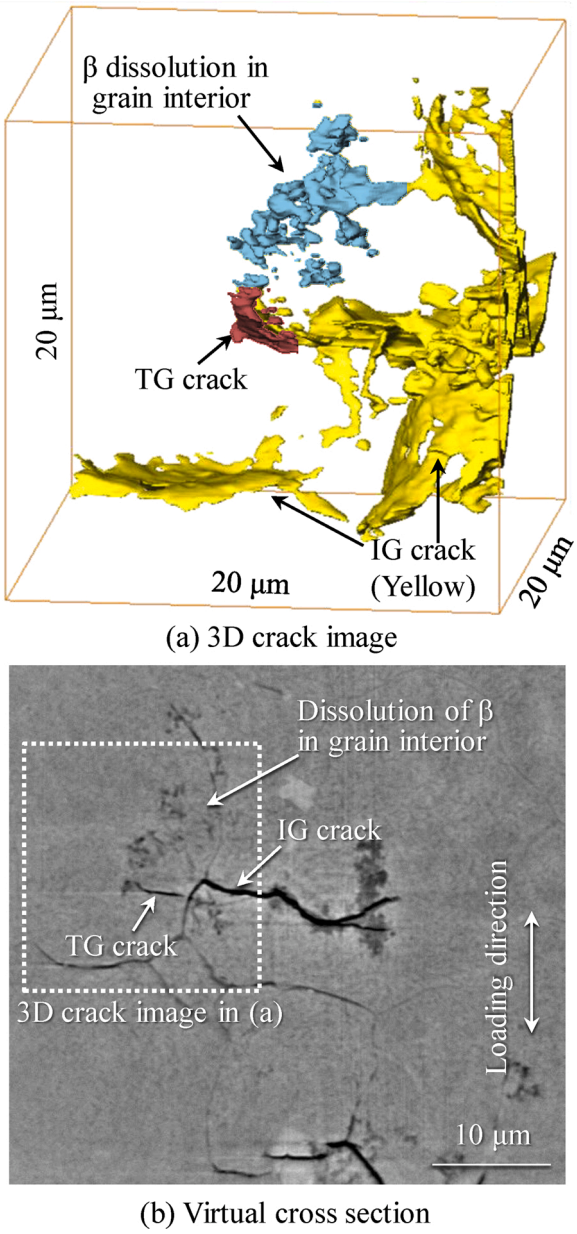

Fig. 14. 3D crack morphology in specimen FLMβ(HS)-HH(WTR), visualized with the imaging-type XMT technique. (a) shows a magnified volume-rendered image corresponding to the white-square region in (b).

estimated to be 4.4 × 10^{-12} mol for the single SCC crack shown in Fig. 17.

The interval between the two scans (with applied strains of 1.2 and 1.5%) was 22 min. Hydrogen can diffuse over 17.4 μm during this time period, assuming a hydrogen diffusion coefficient at room temperature of 2.3 × 10^{-13} m^2/s [56]. Assuming the hydrogen was uniformly distributed from the crack surface up to a distance of 17.4 μm, the average hydrogen content in this region reached 11.7 mass ppm with the addition of the pre-existing hydrogen content of 5.0 mass ppm. Comparison of the total amount of $Al(OH)_3$ (2523.2 μ m^3) with the increment used in the above estimation (250.8 μ m^3) similarly indicates that a larger amount of hydrogen was formed during the initial corrosion pit formation, and may have been residual at the moment of the tensile test. It is also to be noted that $Al(OH)_3$ is soluble in water, implying that the measured amount of $Al(OH)_3$ would be somewhat less than the actual value. It can therefore be inferred that the estimation of local hydrogen content would be fairly conservative, providing a possible lower limit.

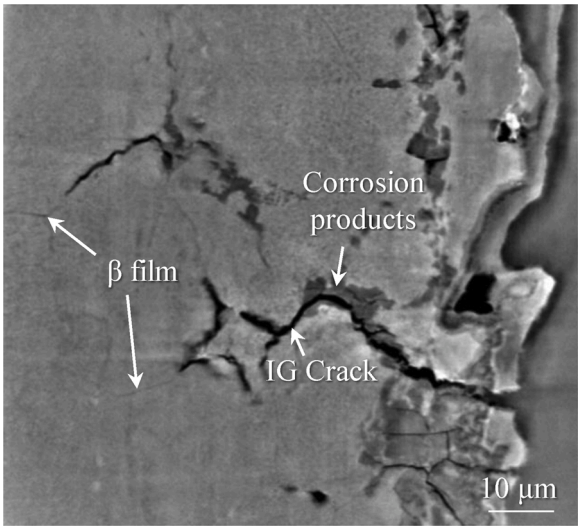

Fig. 15. A virtual cross section of a 3D image captured at $\varepsilon_{appl.} = 1.5\%$, before image segmentation, illustrating a crack and corrosion products in specimen FLMβ(HS)-HH(WTR).

Recently McMahon et al. have investigated hydrogen generation by employing gaseous hydrogen collection testing [36]. They have successfully obtained hydrogen gas volume as a function of applied potential, concluding that the hydrogen gas evolution rate trends with potential are similar to the mass loss rate trends [36]. This is consistent with the assumption in the estimation of hydrogen generation. They however claimed that relating hydrogen gas volume to absorbed atomic hydrogen content is analytically complicated due such as to unknown degree of hydrogen recombination. The present study has for the first time provided such data on the basis of the precise experimental measurements.

5. Discussion

The SCC behavior of Al-Mg alloys have been well documented in the current literature as has been introduced in the introduction section. In this study, the present authors would not intend to repeat it again if it has been also visualized with the direct observations in the present study. Instead, the present authors would like to focus what have been revealed for the first time by directly visualizing the SCC phenomena in this discussion section. The following findings are particularly important;

(1) SCC can occur in Al-Mg alloys only with preexisting hydrogen of 5 mass ppm in concentration without β precipitation (and therefore without its dissolution).
(2) Hydrogen embrittlement process has been verified with supporting experimental evidences with both the plastic strain mapping and CTOD measurement.
(3) As has been reported in the literature, it is true that the film-like β is harmful for SCC in Al-Mg alloys. More catastrophic fracture can however occur when the film-like β is combined with coarse and almost reticulately interconnected plate-like β phase in the grain interior (i.e., material FLMβ(HS)).
(4) The amount of local hydrogen uptake in the course of SCC was for the first time quantitatively measured by devising a set of measurements such as the bubble growth monitoring, the precise 3D measurement of the corrosion product together with its in-situ increment, and the pH measurement for a micro droplet. We can therefore discuss the local criterion for SCC to occur quantitatively for the first time with this information in section 5.1. It will be also utilized for preventing SCC in section 5.2.

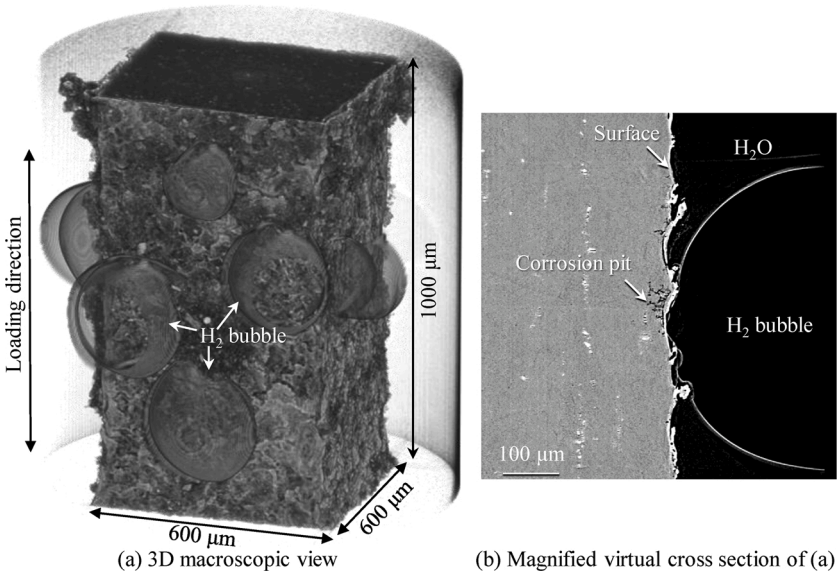

(a) 3D macroscopic view (b) Magnified virtual cross section of (a)

Fig. 16. A 3D image captured with the projection-type XMT technique, representing hydrogen bubble formation during the in-situ tensile testing of specimen FLMβ (HS)-HH(WTR), utilized for the estimation of crack-tip hydrogen uptake: (a) 3D macroscopic view of the overall specimen and surrounding microdroplet; (b) magnified virtual cross section at one of the bubbles in (a), including the corrosion pit that formed the bubble.

5.1. Quantitative assessment of hydrogen embrittlement in inter-β ligaments

In the present study, specimen PTLβ-HH(Ar) exhibited hydrogen embrittlement only with a pre-existing hydrogen content of 5.0 mass ppm. When external hydrogen was continuously absorbed into the specimens during SCC, the local hydrogen content increased to at least 11.7 mass ppm in the case of specimen FLMβ(HS)-HH(WTR), which exhibited extremely brittle fracture for aluminum. Ohnishi et al.'s SCC test of an Al-8Mg alloy with cathodically charged hydrogen [22] showed that SCC life was reduced to roughly 1/1000 of its initial lifetime with an increase in total hydrogen content from 1.0–2.4 mass ppm. On the other hand, in the present study, neither PTLβ-LH(Ar) (0.2 mass ppm) nor Nβ-HH(WTR) (5.0 mass ppm) showed hydrogen embrittlement. Overall, it may be concluded that a combination of β phase and pre-existing and/or external hydrogen gives rise to SCC. Only when the local hydrogen content is extremely high, through a combination of pre-existing and external hydrogen, does SCC occur without the β phase, as shown in the data for specimen Nβ-HH(WTR) (Fig. 9). The decrease in fracture strain was, however, only 24% in this case (Fig. 9). The estimation of locally produced hydrogen (Section 4.2) indicated that a local hydrogen uptake of 6.7 mass ppm would appear to be a possible lower limit, implying that the presence of either pre-existing or external hydrogen (or both) may result in SCC in an Al-Mg alloy with β phase. In sum, it is most likely that the threshold hydrogen content would be around 1 - several mass ppm, and it is reasonable to assume that this threshold value is dependent on the morphology of the β phase, given the observed differences among materials FLMβ(LS), FLMβ(MS), and FLMβ(HS).

5.2. Prevention of SCC

Some prevention methods for the SCC or hydrogen embrittlement of aluminium alloys have been reported in the literature, or otherwise invented and actually utilized in the industry. It can be however inferred that such approaches seem in many cases empirical and phenomenological, and underlying physical mechanisms can be interpreted in many different ways. In the present study, local hydrogen concentration has been quantitatively evaluated for the first time for SCC, which enables to discuss the requirements for SCC to occur on the basis of the recently revealed hydrogen embrittlement mechanisms. The prevention methods for hydrogen embrittlement have been proposed for aluminium alloys to date on the basis of such new findings on hydrogen embrittlement. Not only in the SCC studies, but also in the numerous studies on the hydrogen embrittlement of aluminium alloys in the current literature, the local accumulation of hydrogen has not been experimentally obtained during hydrogen embrittlement or SCC. This is due to the difficulty in visualizing and quantifying hydrogen especially at a microscopic size scale. In the present study, an SCC prevention method is proposed on the basis of the quantitative hydrogen uptake estimation below together with an assumed methodology for realizing it.

It has been shown that hydrogen is partitioned to various trap sites, such as dislocations, vacancies, precipitates, grain boundaries, etc. [49]. It has been reported that the hydrogen trap energy of aluminum grain boundaries is about 0.2 eV/atom, even in the case of Σ3(112), Σ5(012), and Σ9(221) grain boundaries with relatively high energy values [58]. Many microstructural features in aluminum alloys have hydrogen trap energies greater than the grain boundaries; among them, vacancies, coherent and semi-coherent interfaces of precipitates, the inside of dispersion particles, and pores [49]. It is therefore reasonable to assume that the introduction of high hydrogen energy trap sites to Al-Mg alloys may prevent the occurrence, or at least somewhat suppress the severity, of SCC. In fact, Shimizu et al. has successfully suppressed hydrogen embrittlement in Al-Zn-Mg alloys with high Zn content, which have remarkably high susceptibility to hydrogen embrittlement, by dispersing specific intermetallic compound particles (i.e., Al_7Cu_2Fe) [59]. According to their report, Al_7Cu_2Fe has a remarkably high hydrogen trap energy of 0.56 eV, and more than 90% of the hydrogen in the overall material was absorbed into the Al_7Cu_2Fe particles [59]. At the same time, the local hydrogen content at initiation sites of hydrogen embrittlement cracking was effectively reduced. The total hydrogen content of their Al-Zn-Mg alloys was 6.97 mass ppm, which is relatively close to the pre-existing hydrogen content or local hydrogen uptake of the Al-Mg alloys used in the present study. In this case, trap site occupancy of Al_7Cu_2Fe particles is 1.6×10^{-1}%. So it can be inferred that even if the majority of preexisting hydrogen is stored inside the particles, there is still plenty of space to store hydrogen locally generated at nearby β particles. It can therefore be expected that at least if the original hydrogen content is relatively low, and/or the Al-Mg alloy is effectively shielded from environmental water and humid air, the SCC behavior can

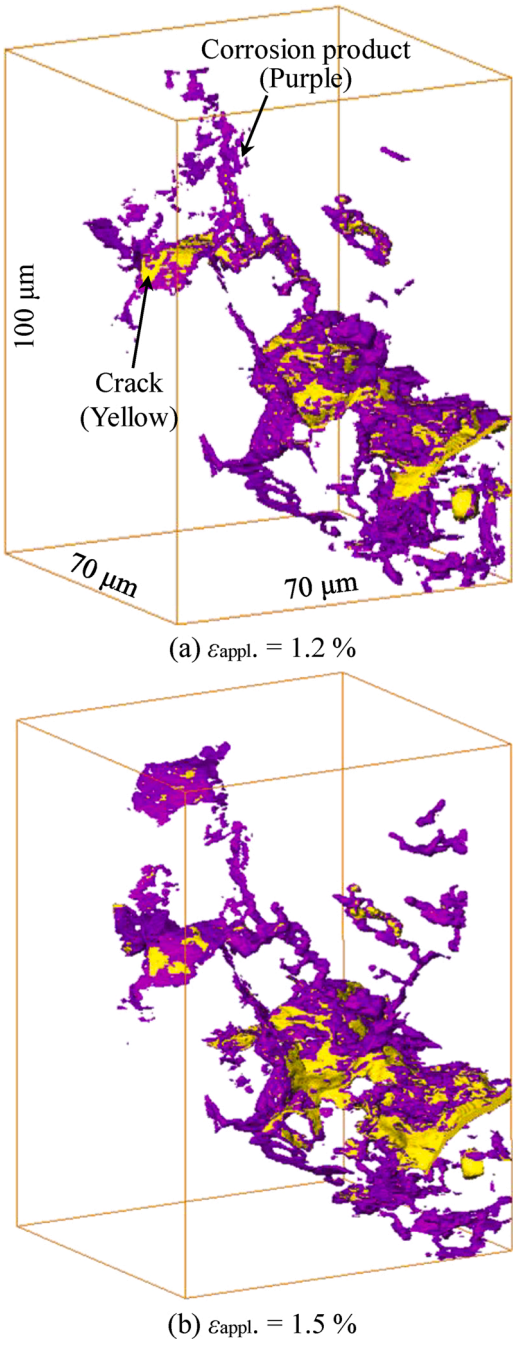

Fig. 17. A set of 3D images after image segmentation, demonstrating crack extension and corrosion product formation in specimen FLMβ(HS)-HH(WTR), between the two neighboring loading steps, utilized for the estimation of crack-tip hydrogen uptake. The cracks and corrosion products are highlighted in yellow and purple, respectively.

be more or less controlled by designing the microstructural features in such a manner.

Conserva et al. added Mn, Cr, and Zr to Al-5~7 Mg alloys to improve SCC, on the supposition that recrystallization and the nucleation of Cr- and Mn-bearing dispersoids on the β phase were potential mechanisms for the improvement experimentally obtained [60]. Meng et al. added Zn to Al-6Mg alloys for the same purpose, and concluded that dispersing grain boundary precipitates and increasing the number of low angle grain boundaries were the main mechanisms for SCC prevention [61]. There is, however, little conclusive evidence in the current literature for these qualitative inferences. In light of the present study's quantitative assessment of inter-β ligament hydrogen embrittlement during SCC (Section 5.1), it can be presumed that some of the dispersed particles may be able to trap hydrogen, thereby reducing the substantial local hydrogen content necessary for inter-β ligament hydrogen embrittlement to occur. As has been reported, first principle simulation readily enables us to determine the exact values of hydrogen trap energy for a variety of intermetallic compounds [59]. Such numerical determinations, combined with pertinent knowledge of crystallographic lattice structure, may enable complementary studies to quantitatively elucidate the true SCC prevention mechanism. Controlling the spatial dispersion, size, and volume fraction of hydrogen trapping microstructural features may enable the development of effective means of preventing SCC in Al-Mg alloys.

6. Summary

Preferential dissolution of the β phase along grain boundaries was observed in 3D in the case of both film-like β phase and discontinuously dispersed β particles. Typical intergranular fracture, representative of the common SSC behavior, was observed in such cases. When the alloy was highly sensitized at 448 K for 100 h (i.e., material FLMβ(HS), coarse precipitates in the grain interior were almost interconnected with each other and nearby grain boundaries. In the most catastrophic SCC, observed after such severe overaging, the fracture mode transitioned from intergranular to half intergranular and half transgranular, and the fracture surface asperity changed from a zig-zag pattern, stemming from the intergranular fracture, to near flatness due to the combination of the two fracture modes.

The subsequent hydrogen embrittlement behavior in the inter-β ligaments was also investigated in detail. A considerable decrease in SCC resistance was measured when the alloys were charged with hydrogen in advance, implying an important role for pre-existing hydrogen in the inter-β ligament fracture. The pre-existing hydrogen content level that caused hydrogen embrittlement was 5.0 mass ppm. At the same time, the added effect of external hydrogen, which was here absorbed from an aqueous solution during loading, was revealed by directly measuring the variation in crack-tip opening displacement along a crack-front line, which is representative of crack-tip plasticity. The effect of external hydrogen was also observable in complex and manifold bifurcation in the crack-tip morphology, which formed even during the short time period of 22 min between neighboring loading steps, due to continuous crack-tip corrosion.

Hydrogen bubble formation and subsequent growth was clearly observed in 3D, with each bubble corresponding to a specific SCC crack. The main corrosion product was identified to be $Al(OH)_3$, according to its linear absorption coefficient in the 3D XMT images. The amount of corrosion product was precisely measured in the 3D XMT images, and the amount of hydrogen produced due to corrosion was estimated with respect to identified anodic, cathodic, and hydrolysis reactions. Hydrogen gas, which was released as molecular gas in the gas bubbles, was also precisely measured using the in-situ imaging technique. The pH value of the aqueous solution was accurately measured during the in-situ tensile testing, enabling estimation of the amount of hydrogen released in the form of hydrogen ions. As a result, the amount of hydrogen uptake during in-situ tensile testing was estimated. It was concluded that the threshold hydrogen content for hydrogen embrittlement to occur in the inter-β ligaments may have been around 1 ~ several mass ppm. Finally, the findings suggest applicability to the development of quantitative means for the prevention of SCC in Al-Mg alloys.

CRediT authorship contribution statement

Kyosuke Hirayama: Writing - original draft, Writing - review & editing, Visualization. **Hiroyuki Toda:** Conceptualization, Methodology, Writing - original draft, Writing - review & editing, Supervision, Project administration. **Dongsheng Fu:** Methodology, Formal analysis,

Investigation, Visualization. **Ryohei Masunaga:** Formal analysis, Investigation, Visualization. **Hang Su:** Investigation. **Kazuyuki Shimizu:** Investigation. **Akihisa Takeuchi:** Resources. **Masayuki Uesugi:** Resources.

Declaration of Competing Interest

The authors declare that they have no known competing financial interests or personal relationships that could have appeared to influence the work reported in this paper.

Acknowledgments

The synchrotron experiments were performed with the approval of JASRI, through proposal numbers 2019A0076, 2018B0076, 2018A0076, 2017B0076, and 2017A0076. One of the authors (HT) is also grateful for the support of the Grant-in-aid for Scientific Research from JSPS, Subject No. 17H01328, and the Light Metal Educational Foundation.

Appendix A. Supplementary data

Supplementary material related to this article can be found, in the online version, at doi:https://doi.org/10.1016/j.corsci.2021.109343.

References

[1] Y. Zhong, M. Yang, Z.-K. Liu, Contribution of first-principles energetics to Al-Mg thermodynamic modelling, Calphad: Computer Coupling Phase Diag. Thermochem. 29 (2005) 303–311.
[2] J.R. Pickens, J.R. Gordon, J.A.S. Green, The effect of loading mode on the stress-corrosion cracking of aluminum alloy 5083, Metall. Trans. A 14A (1983) 925–930.
[3] D. Tanguy, B. Bayle, R. Dif, Th. Magnin, Hydrogen effects during IGSCC of pure Al–5Mg alloy in NaCl media, Corros. Sci. 44 (2002) 1163–1175.
[4] R.K. Viswanadham, T.S. Sun, J.A.S. Green, Grain boundary segregation in Al-Zn-Mg alloys—implications to stress corrosion cracking, Metall. Mater. Trans. A 11 (1980) 85–89.
[5] M.O. Speidel, in: Gibala and Hehemann (Ed.), Hydrogen Embrittlement and Stress Corrosion Cracking of Aluminum Alloys, Hydrogen Embrittlement and Stress Corrosion Cracking, ASM, Metals Park, OH, 1984, pp. 271–296.
[6] J.R. Scully, G.A. Young Jr., S.W. Smith, Hydrogen solubility, diffusion and trapping in high purity aluminum and selected Al-Base alloys, Mater. Sci. Forum 331-337 (2000) 1583–1600.
[7] H.K. Birnbaum, C. Buckley, F. Zeides, E. Sirois, P. Rozenak, S. Spooner, J.S. Lin, Hydrogen in aluminum, J. Alloys Compd. 253–254 (1997) 260–264.
[8] O. Kubaschewski, Gases and metals, American Elsevier for the Metals and Metallurgy Trust, 1970.
[9] L.F. Mondolfo, Aluminum Alloys: Structure and Properties, Butterworths, 1976, p. 296.
[10] W.R. Opie, W.J. Grant, Hydrogen solubility in aluminum and some aluminum alloys, Trans AIME 188 (1950) 1237–1241.
[11] M. Imabayashi, K. Tonda, M. Ouchi, S. Iwamura, On a method for measuring gas content of light alloys, containing volatile constituents, J. Japan Inst. Light Met. 15 (1965) 306–317.
[12] M. Starink, A.-M. Zahra, B' and β precipitation in an Al–Mg alloy studied by DSC and TEM, Acta Mater. 46 (1998) 3381–3397.
[13] P.N.T. Unwin, R.B. Nicholson, The nucleation and initial stages of growth of grain boundary precipitates in Al-Zn-Mg and Al-Mg alloys, Acta Met. 17 (1969) 1379–1393.
[14] M. Conserva, M. Leoni, Effect of thermal and thermo-mechanical processing on the properties of Al-Mg alloys, Metall. Trans. A 6A (1975) 189–195.
[15] C.B. Crane, R.P. Gangloff, Stress corrosion cracking of Al-Mg alloy 5083 sensitized at low temperature, Corros. Sci. 72 (2016) 221–241.
[16] R.H. Jones, J.S. Vetrano, C.F. Windisch Jr., Stress corrosion cracking of Al-Mg and Mg-Al alloys, Corrosion 60 (2004) 1144–1154.
[17] R. Eborall, C.E. Ransley, The reaction of an aluminum magnesium alloy with water vapour, and the adsorption of hydrogen, J. Inst. Metals 71 (1945) 525–552.
[18] T. Ohnishi, Y. Nakatani, Observations of stress corrosion cracking of Al-Mg alloys, J. Japan Inst. Light Met. 27 (1977) 224–231.
[19] G.M. Scamans, A.S. Rehal, Electron metallography of the aluminium-water vapour reaction and its relevance to stress-corrosion susceptibility, J. Mater. Sci. 14 (1979) 2459–2470.
[20] M.E. MacMahon, Z.D. Harris, J.R. Scully, J.T. Burns, The effect of electrode potential on stress corrosion cracking in highly sensitized Al-Mg alloys, Mater. Sci. Eng. A 767 (2019), 138399.
[21] T. Ohnishi, Y. Nakatani, H. Sakamoto, Effect of microstructure on stress corrosion susceptibility of Al-Mg alloy, J. Japan Inst. Light Met. 26 (1976) 8–17.
[22] T. Ohnishi, Y. Nakatani, Effects of hydrogen on stress corrosion cracking of Al-8% Mg alloy, J. Japan Inst. Light Met. 28 (1978) 123–129.
[23] R. Zhang, M.A. Steiner, S.R. Agnew, S.K. Kairy, C.H.J. Davies, N. Birbilis, Experiment-based modelling of grain boundary β-phase (Mg_2Al_3) evolution during sensitisation of aluminium alloy AA5083, Sci. Rep. 7 (2017) 2961.
[24] M.E. McMahon, R.L. Haines, P.J. Steiner, J.M. Schulte, S.E. Fakler, J.T. Burns, Beta phase distribution in Al-Mg alloys of varying composition and temper, Corros. Sci. 169 (2020), 108618.
[25] R.H. Jones, D.R. Baer, M.J. Danielson, J.S. Vetrano, Role of Mg in the stress corrosion cracking of an Al-Mg alloy, Metall. Materl. Trans. A 32A (2001) 1699–1711.
[26] C.B. Crane, R.G. Kelly, R.P. Gangloff, Crack chemistry control of intergranular stress corrosion cracking in sensitized Al-Mg, Corrosion 72 (2016) 242–263.
[27] D. Tanguy, H effects in Al-Mg, Al-Zn-Mg alloys, and Al: experiments, continuum, and atomistic modelling, Corrosion 72 (2016) 297–313.
[28] D.R. Baer, C.F.W, M.H. Engelhard, M.J. Danielson, R.H. Jones, J.S. Vetrano, Influence of Mg on the corrosion of Al, J. Vac. Sci. Technol. A 18 (2000) 131–136.
[29] M.L.C. Lim, R. Matthews, M. Oja, R. Tryon, R.G. Kelly, J.R. Scully, Model to predict intergranular corrosion propagation in three dimensions in AA5083-H131, Mater. Des. 96 (2016) 131–142.
[30] M.E. McMahon, P.J. Steiner, A.B. Lass, J.T. Burns, The effect of temper and composition on the stress corrosion cracking of Al-Mg alloys, Corrosion 73 (2017) 347–361.
[31] S.R. Stock, Recent advances in x-ray microtomography applied to materials, Int. Mater. Rev. 53 (2008) 129–181.
[32] H. Toda, I. Sinclair, J.-Y. Buffière, E. Maire, K.H. Khor, P. Gregson, T. Kobayashi, A 3D measurement procedure for internal local crack driving forces via synchrotron X-ray microtomography, Acta Mater. 52 (2004) 1305–1317.
[33] H. Toda, Z.A.B. Shamsudin, K. Shimizu, K. Uesugi, A. Takeuchi, Y. Suzuki, M. Nakazawa, Y. Aoki, M. Kobayashi, Cavitation during high-temperature deformation in Al–Mg alloys, Acta Mater. 61 (2013) 2403–2413.
[34] H. Toda, K. Uesugi, A. Takeuchi, K. Minami, M. Kobayashi, T. Kobayashi, Three-dimensional observation of nanoscopic precipitates in an aluminum alloy by microtomography with Fresnel zone plate optics, Appl. Phys. Lett. 89 (2006), 143112.
[35] Y. Suzuki, H. Toda, in Advanced Tomographic Methods in Materials Research and Engineering, Oxford University Press, ed. John Banhart, 2008, pp. 181–201.
[36] A. Takeuchi, K. Uesugi, Y. Suzuki, S. Itabashi, M. Oda, Fresnel zone plate with apodized aperture for hard X-ray Gaussian beam optics, J. Synchrotron Rad. 24 (2017) 586–594.
[37] A. Takeuchi, K. Uesugi, M. Uesugi, F. Yoshinaka, T. Nakamura, Nondestructive Multiscale X-Ray Tomography by Combining Microtomography and High-Energy Phase-Contrast Nanotomography, Microsc. Microanal. 24 (2018) 106–107.
[38] K. Hirayama, H. Toda, H. Su, K. Okamura, Y. Suzuki, A. Takeuchi, M. Uesugi, K. Takeda, K. Shimizu, New high-resolution / high-energy X-ray phase-contrast tomography techniques and their applications to structural metals, Acta Mater. (2020) to be submitted.
[39] Md.S. Bhuiyan, Y. Tada, H. Toda, S. Hang, K. Uesugi, A. Takeuchi, Y. Sakaguchi, Watanabe, Influences of hydrogen on deformation and fracture behaviors of high Zn 7XXX aluminum alloys, Int. J. Fract. 200 (2016) 13–29.
[40] G.T. Herman, Image Reconstruction From Projections: the Fundamentals of Computerised Tomography, Academic Press, Orland, FL, 1980.
[41] Y. Kohmura, K. Okada, A. Takeuchi, H. Takano, Y. Suzuki, T. Ishikawa, T. Ohigashi, H. Yokosuka, High spatial resolution hard X-ray microscope using X-ray refractive lens and phase contrast imaging experiments, Nuc. Instr. Mthd. Phys. Res. A 467–468 (2001) 881–883.
[42] W.E. Lorensen, H.E. Cline, Marching cubes: a high resolution 3D surface construction algorithm, Comput. Graph. 21 (1987) 163–169.
[43] H. Toda, E. Maire, Y. Aoki, M. Kobayashi, Three-dimensional strain mapping using in situ X-ray synchrotron microtomography, J. Strain Anal. Eng. Des. 46 (2011) 549–561.
[44] M. Kobayashi, H. Toda, Y. Kawai, T. Ohgaki, K. Uesugi, D.S. Wilkinson, T. Kobayashi, Y. Aoki, M. Nakazawa, High-density three-dimensional mapping of internal strain by tracking microstructural features, Acta Mater. 56 (2008) 2167–2181.
[45] H. Toda, S. Yamamoto, M. Kobayashi, K. Uesugi, H. Zhang, Direct measurement procedure for three-dimensional local crack driving force using synchrotron X-ray microtomography, Acta Mater. 56 (2008) 6027–6039.
[46] H.K. Birnbaum, P. Sofronis, Hydrogen-enhanced localized plasticity—a mechanism for hydrogen-related fracture, Mater. Sci. Eng. A A176 (1994) 191–202.
[47] I.M. Robertson, H.K. Birnbaum, P. Sofronis, in: J.P. Hirth, L. Kubin (Eds.), Dislocations in Solids, vol. 19, Elsevier, New York, 2009, pp. 249–293.
[48] H. Su, H. Toda, R. Masunaga, K. Shimizu, H. Gao, K. Sasaki, MdS. Bhuiyan, K. Uesugi, A. Takeuchi, Y. Watanabe, Influence of hydrogen on strain localization and fracture behavior in AlZnMgCu aluminum alloys, Acta Mater. 159 (2018) 332–343.
[49] H. Su, H. Toda, K. Shimizu, K. Uesugi, A. Takeuchi, Y. Watanabe, Assessment of hydrogen embrittlement via image-based techniques in Al–Zn–Mg–Cu aluminum alloys, Acta Mater. 176 (2019) 96–108.
[50] G. Yi, M.L. Free, Y. Zhu, A.T. Derrick, Capillarity effect controlled precipitate growth at the grain boundary of long-term aging Al 5083 alloy, Metall. Mater. Trans. A 45 (2014) 4851–4862.
[51] M. Kubota, Identification of β phase particles in an isothermally aged Al–10 mass% Mg–0.5 mass% Ag alloy, Mater. Trans. 46 (2005) 2437–2442.
[52] Y. Li, J.M. Cai, L. Guan, G. Wang, pH-dependent electrochemical behaviour of Al3Mg2 in NaCl solution, Appl. Surf. Sci. 467-468 (2019) 619–633.

[53] D. Zhu, W.J. van Ooij, Corrosion protection of AA 2024-T3 by bis-[3-(triethoxysilyl) propyl] tetrasulfide in neutral sodium chloride solution. Part 1: corrosion of AA 2024-T3, Corr. Sci. 45 (2003) 2163–2175.
[54] N.Q. Tuan, A.C. Alves, F. Toptan, A.B. Lopes, A.M.P. Pinto, The effect of Sc and Yb microalloying additions and aged-hardening heat treatment on corrosion behavior of Al–Mg alloys, Mater. Corros. 67 (2016) 60–71.
[55] M. Liu, P. Schmutz, S. Zanna, A. Seyeux, H. Ardelean, G. Song, A. Atrens, P. Marcus, Electrochemical reactivity, surface composition and corrosion mechanisms of the complex metallic alloy Al_3Mg_2, Corros. Sci. 52 (2010) 562–578.
[56] W. Eichenauer, A. Pebler, Measurement of the diffusion coefficient and solubility of hydrogen in aluminum and in copper, Zeitschrift Fur Metallkunde 48 (1957) 373–378.
[57] L.F. Kozin, S.V. Volkov, S.G. Goncharenko, V.V. Permyakov, B.I. Danil'tsev, Kinetics and mechanism of interaction of aluminum and magnesium of Al-Mg-Bi ternary system with water, Prot. Met. Phys. Chem. Surf. 47 (2011) 171–180.
[58] M. Yamaguchi, K. Ebihara, M. Itakura, T. Tsuru, K. Matsuda, H. Toda, First-principles calculation of multiple hydrogen segregation along aluminum grain boundaries, Comput. Mater. Sci. 156 (2019) 368–375.
[59] M. Yamaguchi, T. Tsuru, K. Ebihara, M. Itakura, K. Matsuda, K. Shimizu, H. Toda, Hydrogen trapping in Mg_2Si and Al_7FeCu_2 intermetallic compounds in aluminum alloy: a first-principles calculations, Mater. Trans. (2020) to be submitted.
[60] M. Conserva, M. Leoni, Effect of thermal and thermo-mechanical processing on the properties of Al–Mg alloys, Metall. Mater. Trans. A 6A (1975) 189–195.
[61] C. Meng, D. Zhang, L. Zhuang, J. Zhang, Correlations between stress corrosion cracking, grain boundary precipitates and Zn content of Al–Mg–Zn alloys, J. Alloys Compd. 655 (2016) 178–187.